S1 Flow chart of the instruments

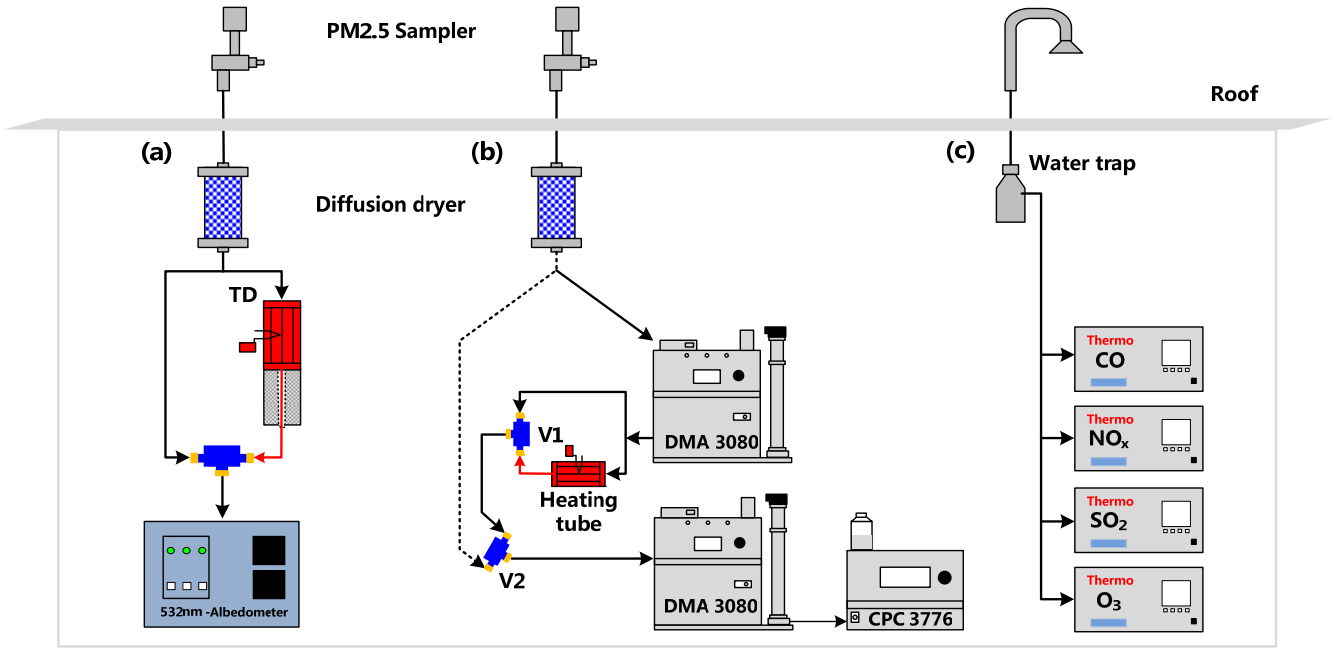

Figure S1: Experimental set-up for the measurements of: (a) aerosol optical properties, (b) volatility of $PM_{2.5}$ particles, and (c) concentrations of pollutant gases.

S2 Estimation of the truncation error of the cavity-enhanced albedometer

The geometry of the cavity-enhanced albedometer is shown in Fig. S2. The inner diameters of the integrating sphere (L) and the truncation reduction tube (d) were 150 mm and 19 mm, respectively. The length of the sample occupied in the truncation reduction tube (l) was ~ 197 mm. Z is the distance of the particle from the scattering location in the sphere to the exit or entrance aperture of the sphere (Z = 0 is for the centre of the sphere).

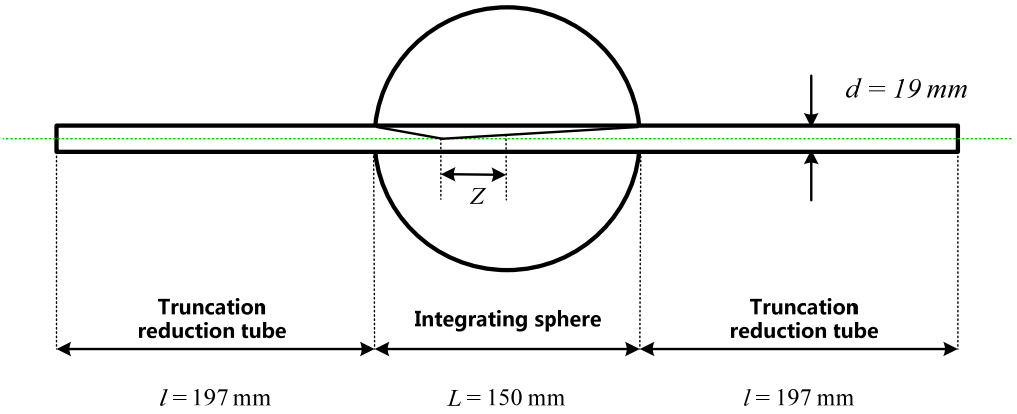

Figure S2 Sample cell geometry of the cavity-enhanced albedometer.

The albedometer truncation error was evaluated with Mie theory by considering the geometry of the cell and the scattering phase function of spherical particles (Moosmüller and Arnott, 2003; Zhao et al., 2014; Onasch et al., 2015). The scattering truncation of the particles with a certain diameter (D) inside the cell ($T(D, \theta)$) is defined as the ratio of the integrated scattering efficiencies of the effective truncation angles to the total scattering efficiency, which can be expressed as following (Onasch et al., 2015):

$$T(D,\theta) = \int_{\theta_1}^{\theta_2} \frac{2I(D,\theta)}{\chi^2 Q_{sca}(m,x,\lambda)} \sin(\theta) d\theta \tag{S1}$$

where θ_1 and θ_2 are the effective truncation angles, $I(D, \theta)$ is the unpolarized scattering intensity, m is the complex refractive index (CRI, $m = n + ik$), λ is the wavelength of incident light, $x = \pi D/\lambda$ is the size parameter, and $Q_{sca}(m,x,\lambda)$ is the scattering efficiency.

The effective truncation angle (θ) depends upon the position of particles within the cell, which can be expressed as (Varma et al., 2003; Zhao et al., 2014):

$$\theta_1(Z) = \tan^{-1}\left(\frac{d/2}{L/2+Z}\right),\ \theta_2(Z) = \tan^{-1}\left(\frac{d/2}{-L/2-Z}\right) \tag{S2}$$

The total scattering truncation can be written as follows (Onasch et al., 2015):

$$T(D)=\int_{Z_1}^{Z_2}\int_{\theta_1(Z)}^{\theta_2(Z)}\frac{2I(D,\theta)}{\chi^2 Q_{sca}(m,x,\lambda)}\sin(\theta)d\theta dZ \quad \text{(S3)}$$

where the end points of Z integration are defined as:

$$Z_1=-\frac{1}{2}L-l\,,\ Z_2=\frac{1}{2}L+l \quad \text{(S4)}$$

A plot of the total scattering truncation of PSL particles with different diameters of our cavity-enhanced albedometer and that of PM_{ssa} reported by Onasch et al. (2015) is shown in Fig S3. By using longer truncation reduction tubes and larger inner diameter integrating sphere, the truncation losses of our albedometer are smaller than that of CAPS PM_{SSA} monitors.

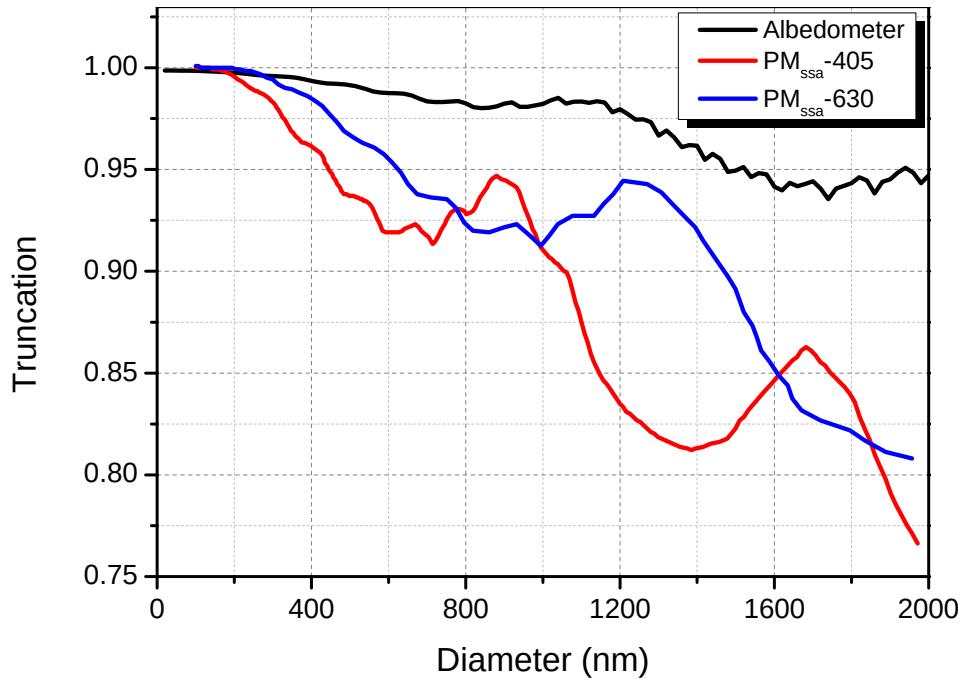

Figure S3 Comparison of the scattering truncations for PSL particles of our albedometer (at λ = 532 nm) and that for CAPS PM_{ssa} (at λ = 405, 630 nm). The complex refractive index of PSL was set to be 1.59 + *i* 0.0.

Three different CRI values were used to represent the scattering truncation of different-type particles: the non-absorbing (1.55 + *i* 0); absorbing (1.55 + *i* 0.01); and strongly absorbing (1.85 + *i* 0.71) particles (treated as black carbon). As shown in Fig. S4, the calculated truncations decreased with increasing of particle size and imaginary part of CRI.

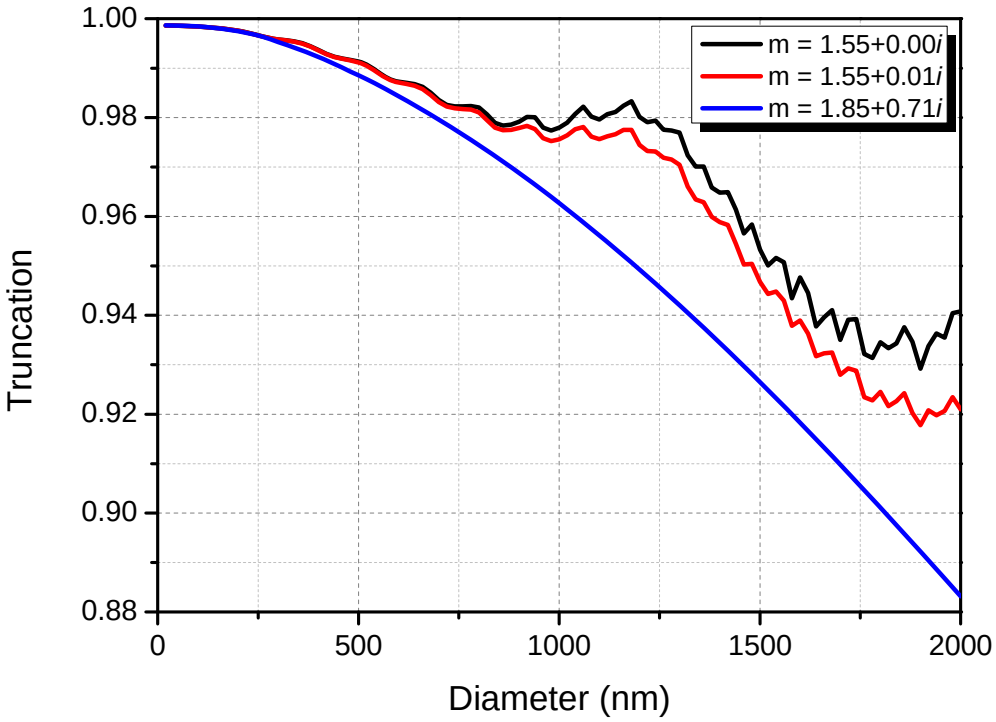

Figure S4 Scattering truncation calculated by the Mie model for three different type particles at λ = 532 nm.

The accumulative truncation errors (ATE) based on the SMPS data (integrated with the normalized number size distribution of ambient aerosol) can be expressed as follows:

$$ATE = \int f(D_i)(1-T(D_i))dD_i \quad \text{(S5)}$$

where D_i is the particle diameter, $f(D_i)$ is the normalized particle number distribution, $T(D_i)$ is the scattering truncation of the corresponding diameter. As shown in Fig. S5, the accumulative truncation errors for three different type particles are all smaller than 0.2 %. Thus, the truncation errors of the measured scattering coefficients were negligible for fine particles in this work.

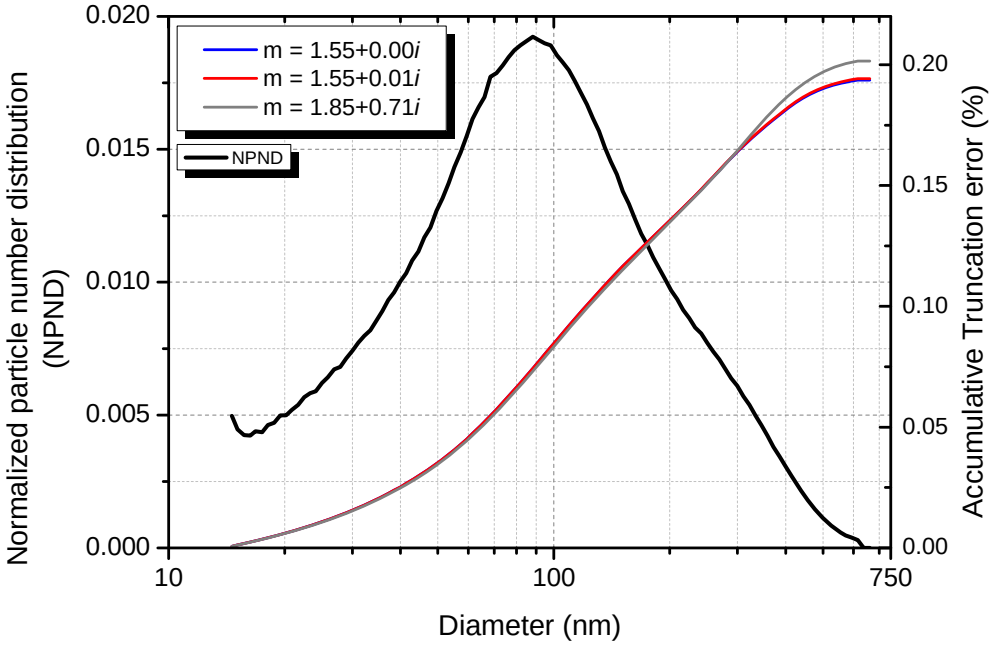

Figure S5 Averaged normalized particle number distribution during the observation period and the corresponding accumulative truncation errors at each size.

S3 Particle losses inside the thermodenuder

Laboratory-generated polydisperse NaCl particles (with TSI 3076 constant output atomizer) were used to estimate the particle losses inside the thermodenuder (TD). Particles were dried to RH < 5% with a silica gel diffusion dryer (TSI 3062), neutralized with an aerosol neutralizer (TSI 3077), and then diluted with a buffer to obtain a stable aerosol concentration. The size resolved TD losses are shown in Fig. S6. The measured particle losses agreed with manufactory given data (Dekati Ltd., Technical Note, 2001).

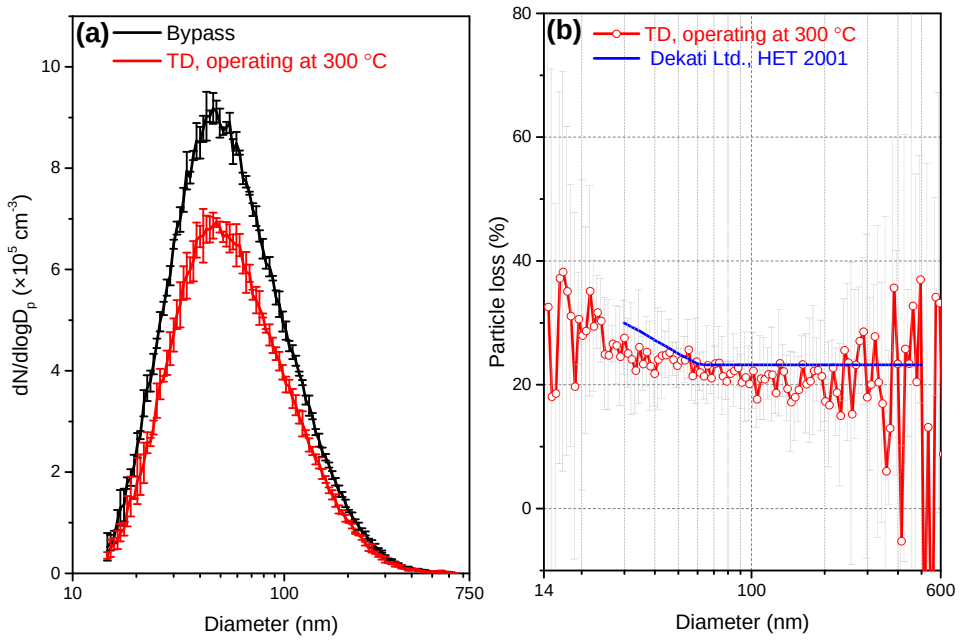

Fig. **S6:** (a) The changes of particle number distribution of NaCl particles passed through the bypass and the TD operating at 300 °C. (b) Size resolved particle losses of the TD. Manufactory given losses (blue line, Dekati Ltd., HET. 2001) are also shown in the figure.

Due to the small absorption cross section, the contribution of small particle to aerosol absorption is negligible. Particle number losses may not exactly the same as the optical losses. In this work, laboratory-generated polydisperse NaCl particles and ambient sample before and after passing through of the TD were used to estimate the actual optical losses inside the TD. The corresponding measured extinction and scattering coefficients for NaCl are shown in the upper panel of Fig. S7. The TD loss was estimated to be ~ 26% for both scattering and extinction. The results for ambient sample were shown in

the lower panel of Fig. S7. The TD losses for both channels were estimated to be ~ 32%, which are comparable to the estimated losses of absorption of black carbon (32 ± 3% at λ = 370 nm, and 24 ± 6% at λ = 880 nm) (Devi et al., 2016). In this work, we use actual TD loss of ambient aerosol 32% for further data analysis.

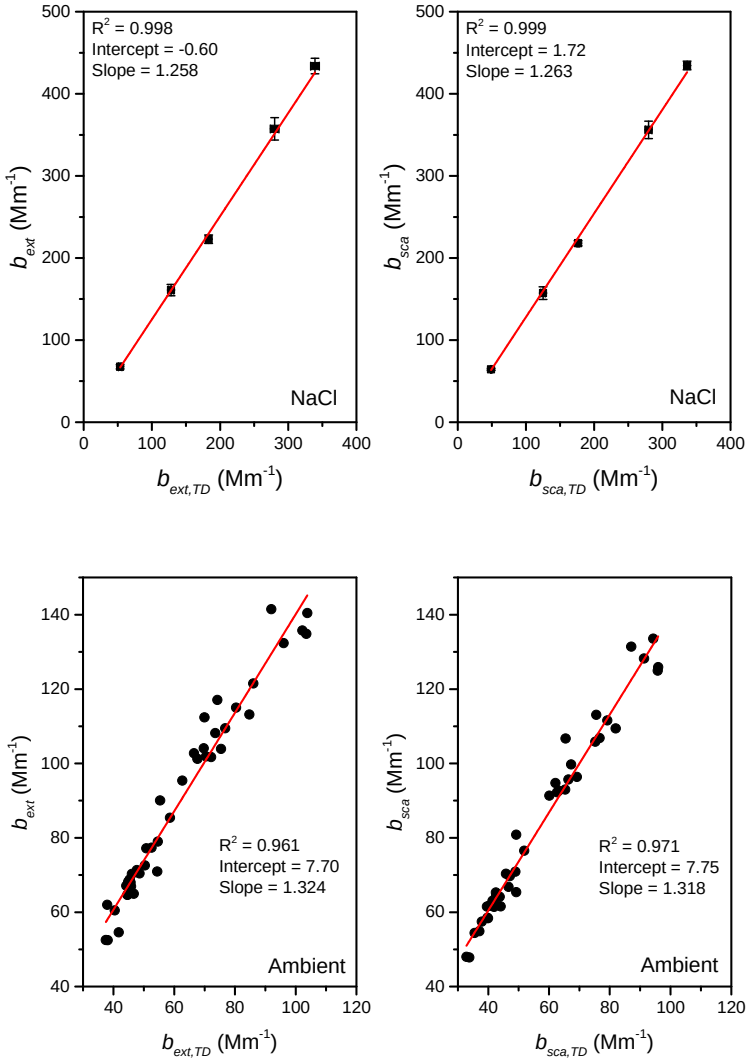

Figure S7: Scatter plot of the measured extinction and scattering coefficients of NaCl (upper panel, operating at 300 °C) and ambient particles (lower panel, operating at room temperature) before ($b_{ext,scat}$) and after ($b_{ext,scat,\,TD}$) passing through the TD.

S4 Meteorological parameters during the measurement period

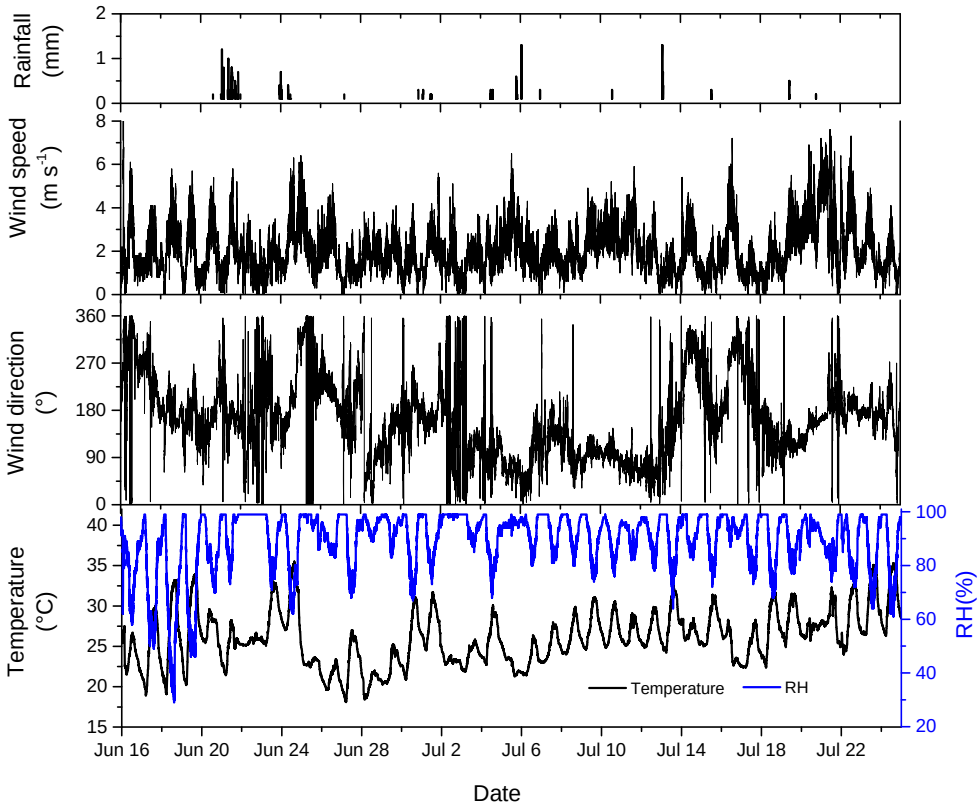

Figure S8: Time profiles of rainfall, wind speed, wind direction, temperature, and relative humidity (RH) during the measurement period.

S5 Air mass backward trajectory

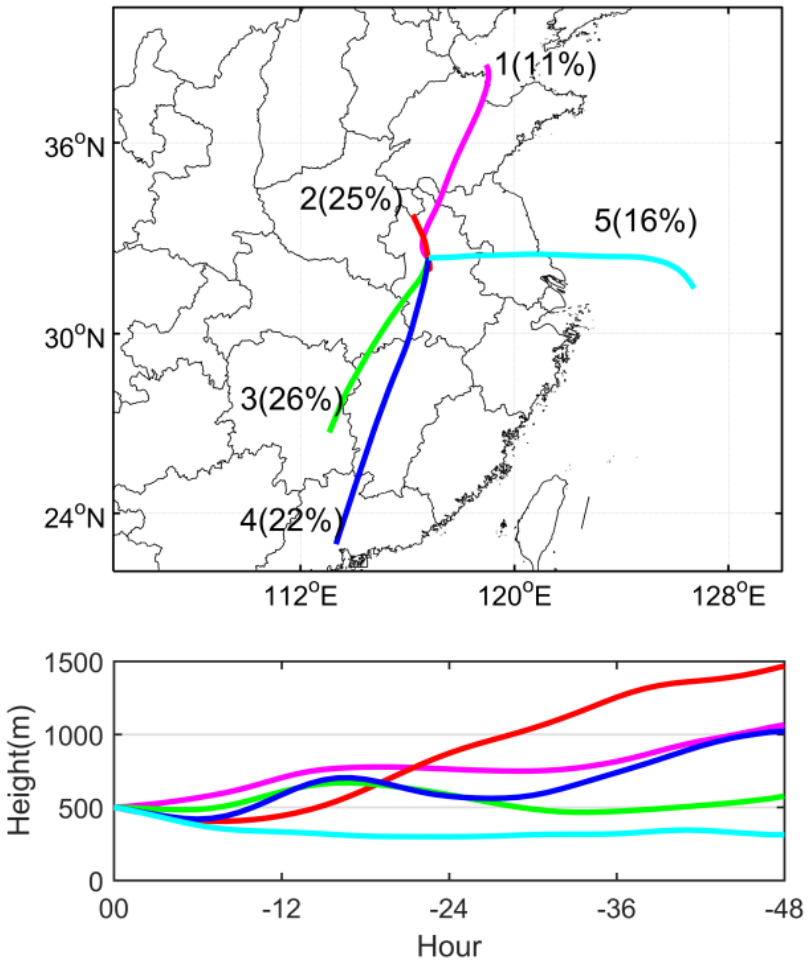

Figure S9: The 48 h back trajectories ending at 500 m above ground level at the Shouxian site (calculated every 1 h) were classified into five groups using the clustering method given by HYSPLIT model.

S6 Mie theory modelling and attribution of light absorption

A graphical representation of the calculation procedure is shown in Fig. S10. Comparisons of modeling and observation E_{abs} and SSA are shown as a scatter plot in Fig. S11.

The calculation of the model is as follows:

(a) Initial inputs parameters are the diameter of BC core (D_{core}), CRI of core (m_{BC}) and real part of the CRI of shell (n_{shell});

In this work, m_{BC} at λ= 532 nm was fixed at 1.85 +i 0.71, and n_{shell} was fixed at 1.55 (Bond et al., 2006; Lack et al., 2012; Saleh et al., 2015). k_{shell} varied from 0 (non-absorbing coating; clear shell) to 0.1 (strongly absorbing coating) (Lack and Cappa., 2010). D_{core} was constrained between 50 and 400 nm, while D_{shell} ranged from 50 (for thinly coated BC) to 800 nm (for thickly coated BC).

(b) Calculate the extinction, scattering and absorption coefficients (b_{ext}, b_{sca}, and b_{abs}) of the BC core and coated particles with different k_{shell} and D_{shell} using the core-shell model;

(c) Calculate E_{abs} and ω from the calculated b_{ext}, b_{sca}, and b_{abs} of bare BC and coated particles;

(d) Determine a set of optimized D_{shell} and k_{shell} values by minimizing the "merit function", χ^2:

$$\chi^2 = \frac{(\omega - \omega_{calc})^2}{\varepsilon_{\omega}^2} + \frac{(E_{abs} - E_{abs,calc})^2}{\varepsilon_{E_{abs}}^2} \quad \text{(S1)}$$

Here, ω and E_{abs} are the observed values, ω_{calc} and $E_{abs,calc}$ are the corresponding calculated values, and ε_{ω} and ε_{Eabs} are the measurement uncertainties of ω and E_{abs}, respectively.

(e) The outputs of (d) are the optimized D_{shell}, k_{shell}, $E_{abs,calc}$ and ω_{calc} for a given D_{core} in (a). A linear fit (as shown in Fig. S11) of the calculated and observed E_{abs} and ω with different D_{core} was performed. A lookup table (in 10 nm step increments) was built to find the optimized D_{core} (bold text in the supplement Table S1). In this work, the optimized D_{core} was determined to be 160 nm. This result falls within the diameter range of 120 - 165 nm reported by Wu et al. (2018), as well as the SP2 measurement results of rBC, which ranged from 110 – 220 nm in different megacities in China (Huang et al., 2011; Wang et al., 2015; Gong et al, 2016; Wu et al., 2018).

Table S1: Lookup table of the linear fit (intercept, slope, and R^2) of calculated and observed E_{abs} and ω for different BC core diameters (D_{core}).

D_{core} (nm)	Intercept-E_{abs}	Slope-E_{abs}	R^2-E_{abs}	Intercept-ω	Slope-ω	R^2-ω
50	0.6936	0.7268	0.9283	-0.076	1.0874	0.9681
60	1.1900	0.5496	0.8872	-0.0917	1.1044	0.9764
70	1.3963	0.4697	0.8363	-0.0865	1.0982	0.9746
80	1.1822	0.5455	0.8273	-0.0439	1.0498	0.9857
90	0.7284	0.7126	0.9007	-0.0022	1.0025	0.9899
100	0.1847	0.9277	0.9716	-0.0247	1.0284	0.9955
110	-0.0062	1.0051	0.9953	0.0055	0.9938	0.9974
120	0.0221	0.9905	0.9975	0.0047	0.9946	0.9983
130	0.0204	0.9913	0.9982	-0.001	1.0012	0.9992
140	-0.0050	1.0013	0.9988	-0.0052	1.0059	0.9990
150	0.0050	0.9975	0.9981	-0.0030	1.0035	0.9995
160	**-0.0061**	**1.0027**	**0.9988**	**-0.0000**	**1.0003**	**0.9995**
170	-0.0125	1.0055	0.9986	-0.0034	1.0039	0.9996
180	-0.0013	1.0060	0.9990	0.0088	0.9900	0.9995
190	0.0042	0.9984	0.9990	0.00310	0.9965	0.9994
200	0.0007	0.9998	0.9994	-0.0022	1.0025	0.9994
210	0.0081	0.9967	0.9992	0.0058	0.9933	0.9998
220	0.0126	0.9950	0.9994	0.0033	0.9962	0.9997
230	-0.0194	1.0088	0.9992	-0.0034	1.0039	0.9998
240	0.0104	0.9947	0.9995	0.0015	0.9982	0.9998
250	-0.0001	0.9996	0.9994	0.0003	1.0004	0.9998
260	0.0116	0.9951	0.9993	0.0020	0.9977	0.9998
270	0.0108	0.9956	0.9988	-0.0034	1.0040	0.9996
280	0.1358	0.9383	0.9913	0.0063	0.9926	0.9994
290	0.2722	0.8780	0.9741	0.0170	0.9803	0.9988
300	0.4059	0.8171	0.9470	0.0181	0.9790	0.9986
310	0.6670	0.6987	0.9182	0.0342	0.9602	0.9973
320	0.9994	0.5477	0.8223	0.0528	0.9386	0.9946
330	1.3743	0.3769	0.5716	0.0697	0.9188	0.9911
340	1.7566	0.1994	0.2040	0.0876	0.8980	0.9863
350	2.0968	0.0364	-0.0366	0.1099	0.8717	0.9846

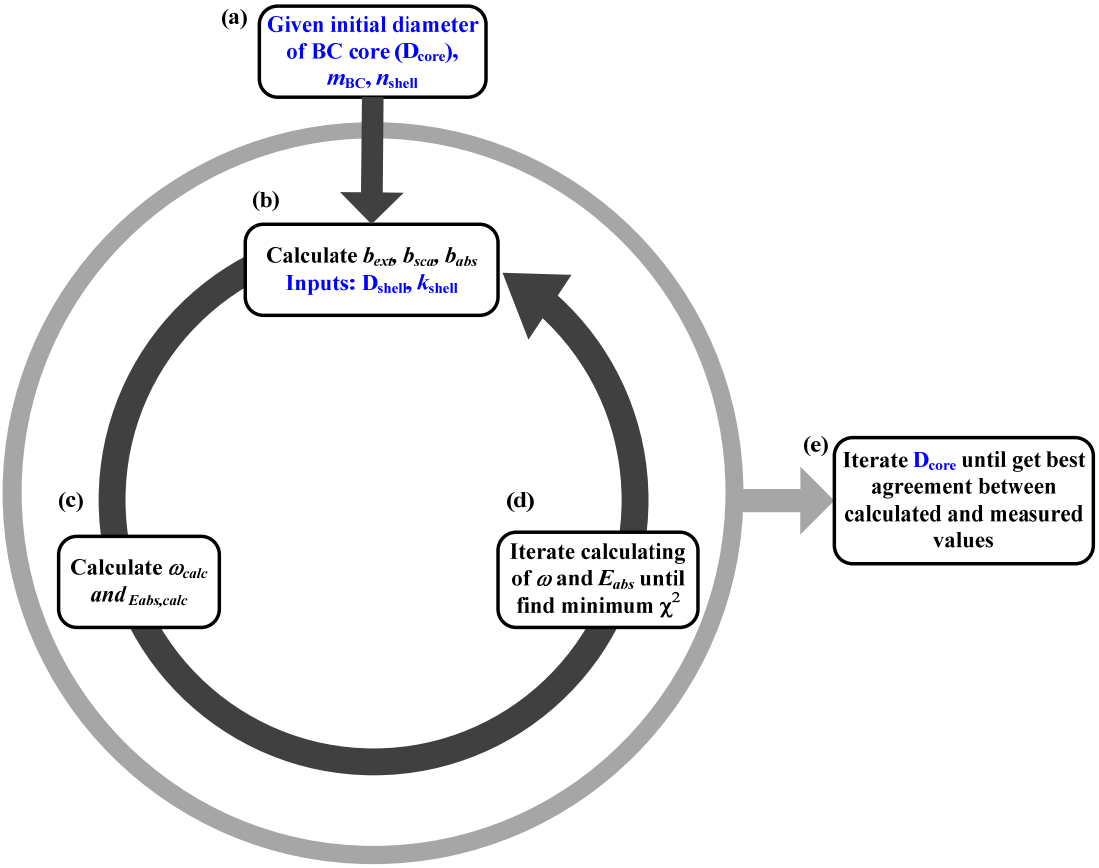

Figure S10 Optimization process for determining core (D_{core}) and shell (D_{shell}) diameters, and the imaginary part of CRI of the shell (k_{shell}).

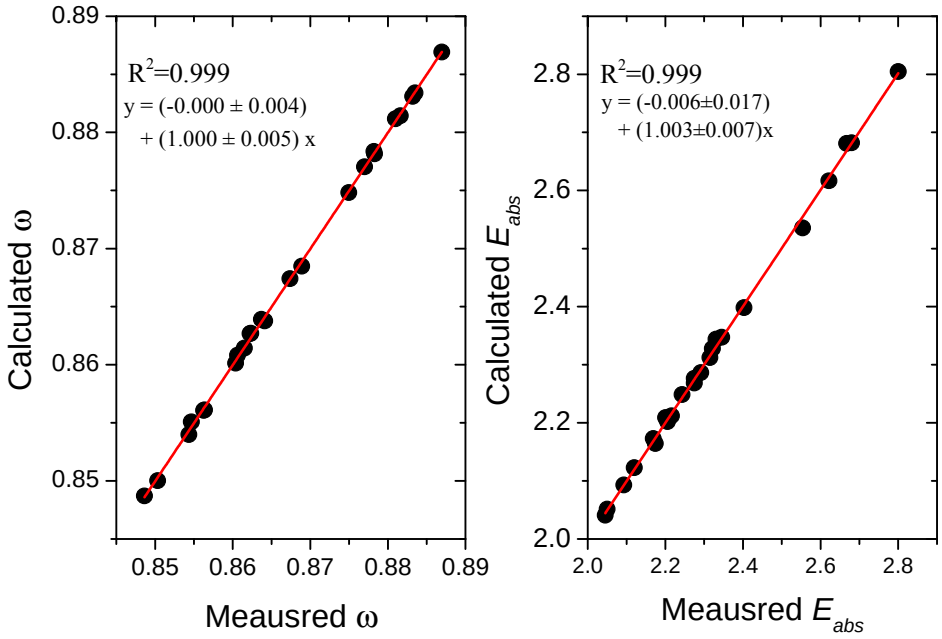

Figure S11 The comparisons of the measured and calculated E_{abs} and ω.

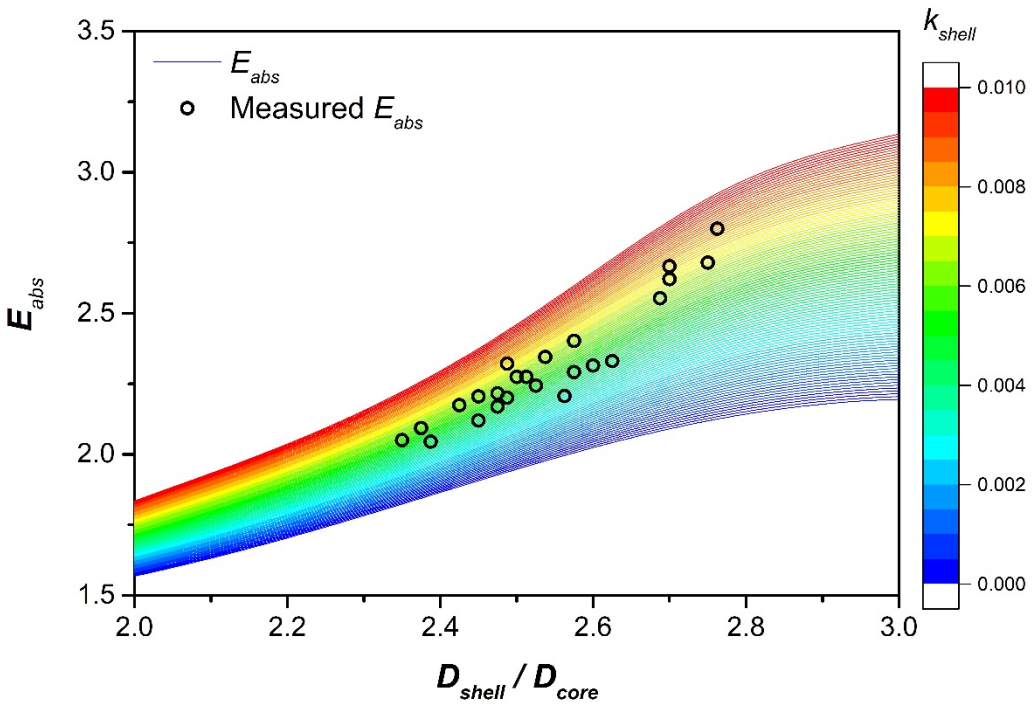

Figure S12 The plot of measured and modelled E_{abs} values with different D_{shell}/D_{core}. D_{core} is fixed at 160 nm, and D_{shell} is ranged from 320 to 480 nm. The imaginary parts (k_{shell}) of complex refractive index ranged from 0 to 0.01 respectively present the clear and brown shell.

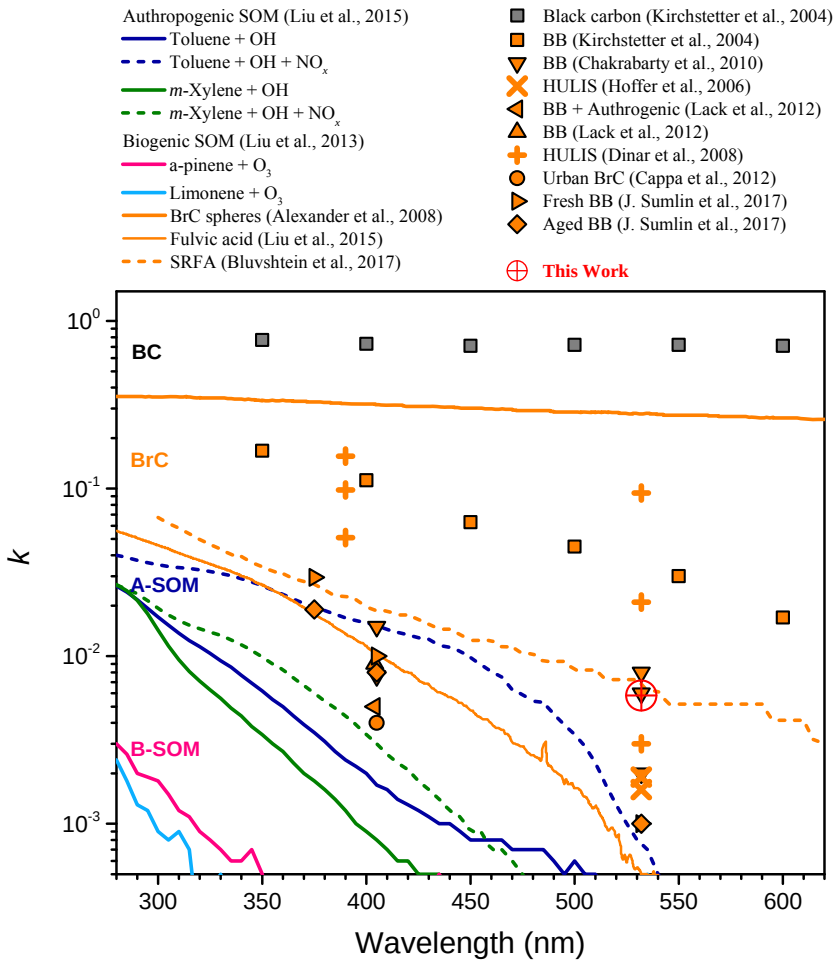

Figure S13: Comparison of the retrieved imaginary part of the coated shell with previously reported values of fresh and aged organic material (adapted from P. Liu et al. (2015) and J. Sumlin et al. (2017)).

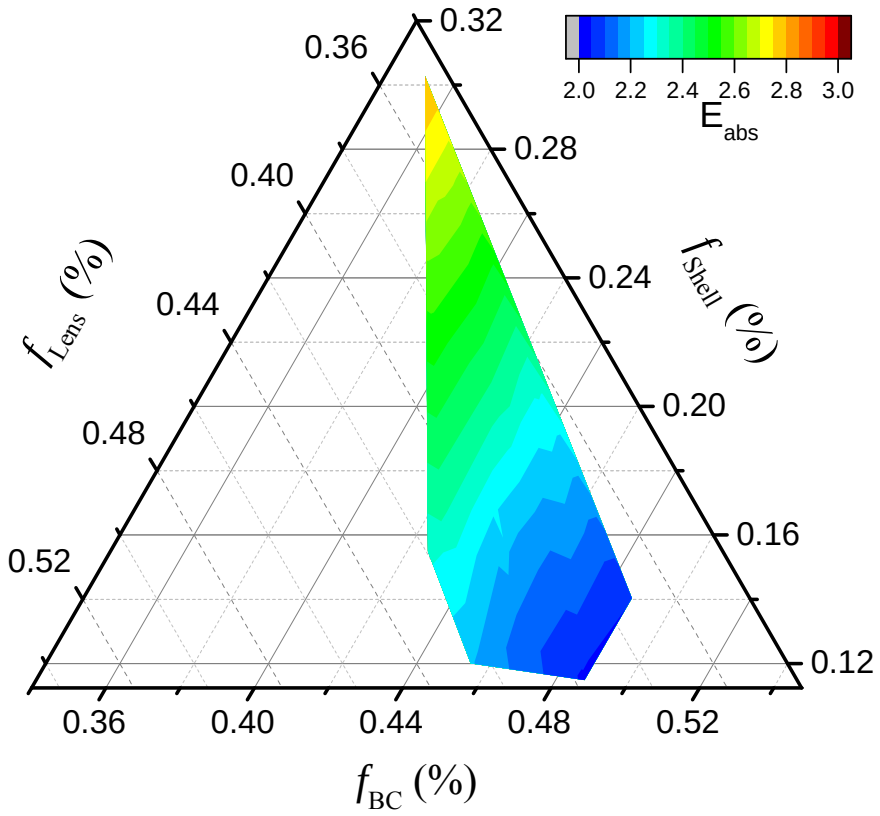

Figure S14: Ternary plot of the fractional contribution of lensing effect (f_{Lens}), the absorption of BC (f_{BC}) and the shell (f_{Shell}) to absorption enhancement (the values of E_{abs} were color-coded).

References:

Bond, T. C., and Bergstrom, R. W.: Light Absorption by Carbonaceous Particles: An Investigative Review, Aerosol Sci. Technol., 40, 27-67, doi:10.1080/02786820500421521, 2006.

Dekati Ltd., HET. (2001). Sampling automotive exhaust with a thermodenuder. Dekati Ltd., Technical Note.

Devi, J. J., Bergin, M. H., Mckenzie, M., Schauer, J. J. and Weber, R. J.: Contribution of particulate brown carbon to light absorption in the rural and urban Southeast US, Atmos. Environ., 136, 95-104, 2016.

Gong, X., Zhang, C., Chen, H., Nizkorodov, S. A., Chen, J., and Yang, X.: Size distribution and mixing state of black carbon particles during a heavy air pollution episode in Shanghai, Atmos. Chem. Phys., 16, 5399-5411, doi: 10.5194/acp-16-5399-2016, 2016.

Huang, X. F., He, L. Y., Hu, M., Canagaratna, M. R., Kroll, J. H., Ng, N. L., Zhang, Y. H., Lin, Y., Xue, L., Sun, T. L., Liu, X. G., Shao, M., Jayne, J. T., and Worsnop, D. R.: Characterization of submicron aerosols at a rural site in Pearl River Delta of China using an Aerodyne High-Resolution Aerosol Mass Spectrometer, Atmos. Chem. Phys., 11, 1865-1877, doi:10.5194/acp-11-1865-2011, 2011

Lack, D. A., and Cappa, C. D.: Impact of brown and clear carbon on light absorption enhancement, single scatter albedo and absorption wavelength dependence of black carbon, Atmos. Chem. Phys., 10, 4207-4220, doi: 10.5194/acp-10-4207-2010, 2010.

Lack, D. A., Langridge, J. M., Bahreini, R., Cappa, C. D., Middlebrook, A. M., and Schwarz, J. P.: Brown carbon and internal mixing in biomass burning particles, Proc. Natl. Acad. Sci. U S A, 109, 14802-14807, doi: 10.1073/pnas.1206575109, 2012.

Liu, P. F., N. Abdelmalki, H.-M. Hung, Y. Wang, W. H. Brune, and S. T. Martin,: Ultraviolet and visible complex refractive indices of secondary organic material produced by photooxidation of the aromatic compounds toluene and m-xylene, Atmos. Chem. Phys., 15, 1435–1446, doi:10.5194/acp-15-1435-2015, 2015.

Moosmüller, H., and Arnott, W.P.: Angular Truncation Errors in Integrating Nephelometry, Rev. Sci. Instrum. 74:3492-3501, 2003.

Onasch, T.B., Massoli, P., Kebabian, P.L., Hills, F.B., Bacon, F.W., and Freedman, A.: Single Scattering Albedo Monitor for Airborne Particulates, Aerosol Sci. Technol. 49:267-279, 2015.

Saleh, R., Marks, M., Heo, J., Adams, P. J., Donahue, N. M., and Robinson, A. L.: Contribution of brown carbon and lensing to the direct radiative effect of carbonaceous aerosols from biomass and biofuel burning emissions, J. Geophys. Res. Atmos., 120, 10, 285-10, 296, doi:10.1002/2015JD023697, 2015.

Sumlin, B. J., Pandey, A., Walker, M. J., Pattison, R. S., Williams, B. J., and Chakrabarty, R. K.: Atmospheric photooxidation diminishes light absorption by primary brown carbon aerosol from biomass burning, Environ. Sci. Tech. Lett., 4, 540-545, doi: 10.1021/acs.estlett.7b00393, 2017.

Varma, R., Moosmüller, H., and Arnott, W. P.: Toward an ideal integrating nephelometer, Opt. Lett., 28, 1007–1009, 2003.

Wang, Q. Y., Huang, R.-J., Cao, J. J., Tie, X. X., Ni, H. Y., Zhou, Y. Q., Han, Y. M., Hu, T. F., Zhu, C. S., Feng, T., Li, N., and Li, J. D.: Black carbon aerosol in winter northeastern Qinghai–Tibetan Plateau, China: the source, mixing state and optical property, Atmos. Chem. Phys., 15, 13059-13069, doi:10.5194/acp-15-13059-2015, 2015.

Wu, C., Wu, D., and Yu, J. Z.: Quantifying black carbon light absorption enhancement with a novel statistical approach, Atmos. Chem. Phys., 18, 289-309, https://doi.org/10.5194/acp-18-289-2018, 2018.

Zhao, W., Xu, X., Dong, M., Chen, W., Gu, X., Hu, C., Huang, Y., Gao, X., Huang, W., and Zhang, W.: Development of a cavity-enhanced aerosol albedometer, Atmos. Meas. Tech., 7, 2551–2566, 2014.